JOURNAL OF GEOPHYSICAL RESEARCH, VOL. 96, SUPPLEMENT, PAGES 19,153–19,169, OCTOBER 30, 1991

Remote Sensing of Neptune's Bow Shock: Evidence for Large-Scale Shock Motions

IVER H. CAIRNS,[1] CHARLES W. SMITH,[2] WILLIAM S. KURTH,[1]
DONALD A. GURNETT,[1] AND STEWART MOSES[3]

The Voyager 2 spacecraft observed high levels of Langmuir waves before the inbound crossing of Neptune's bow shock, thereby signifying magnetic connection to the bow shock. The Langmuir waves occurred in multiple bursts throughout two distinct periods separated by an 85-min absence of wave activity. We use the times of onsets, stable maxima, and disappearances of the waves, together with the magnetic field direction and spacecraft position, to perform a "remote-sensing" analysis of the shape and location of Neptune's bow shock prior to the inbound bow shock crossing. The bow shock is assumed to have a paraboloidal shape (symmetric about the Sun-Neptune line) with a standoff distance and flaring parameter determined independently for pairs of wave events. Our analyses show that published static models for the location of Neptune's bow shock cannot explain the wave data. Instead, the nose of Neptune's bow shock is located near 38–43 R_N during the first wave period and moves monotonically planetward from 38.5 R_N to 34.5 R_N during the second wave period. The remote-sensing analysis gives a shock position consistent with the time of the inbound shock crossing and an average flaring parameter consistent with the inbound and outbound shock crossings. Location of the shock's nose near 38–43 R_N during the first wave period is consistent with the observed variations in the solar wind ram pressure. Measured variations in the magnetic field direction and ram pressure explain the magnetic disconnection of the spacecraft from the shock during the period without observed Langmuir waves. However, the analysis indicates that the shock's nose moved continuously planetward during the second wave period while the ram pressure remained effectively constant. As normalized by the ram pressure, the remotely sensed shock moves sunward during the first wave period and planetward in the second wave period. The maximum standoff distance occurs while the dipole's axis is close to being perpendicular to the Sun-Neptune direction. One interpretation of these results is that the location of Neptune's bow shock is controlled by the rotation phase of Neptune's oblique, tilted dipole. Our analyses should permit testing of detailed theoretical models for changes in the position and shape of Neptune's bow shock with rotation phase and solar wind ram pressure variations.

1. INTRODUCTION

Electron plasma waves, commonly called Langmuir waves, have provided the first evidence for a bow shock at each of the outer planets visited by the Voyager spacecraft [*Scarf et al.*, 1979; *Gurnett et al.*, 1981*a*, 1986, 1989]. Neptune was no exception. Approximately 4 hours before crossing Neptune's bow shock the plasma wave receiver (PWS instrument) on the Voyager 2 spacecraft first observed waves identified as Langmuir waves [*Gurnett et al.*, 1989]. These waves were then observed intermittently until Voyager passed through Neptune's bow shock near 1445 spacecraft event time (SCET), August 24, 1989. Subsequent comparison with the ion density measured by the Voyager plasma (PLS) instrument confirmed that these waves had frequencies near the electron plasma frequency, as expected for Langmuir waves.

The standard model for generation of these waves involves electrons accelerated at the quasi-perpendicular regions of the bow shock, near the tangent point, streaming away from the shock along the magnetic field and driving the waves by the ordinary two-stream or bump-on-tail instability [*Scarf et al.*, 1971; *Filbert and Kellogg*, 1979; *Cairns*, 1987*a*, *b*; *Gurnett et al.*, 1989, and references therein]. Accordingly, the presence of the waves is interpreted in terms of the spacecraft being magnetically connected to a region of the shock near the tangent point which is producing energetic electrons. By assuming magnetic connection of the spacecraft to the tangent point when the waves appear, disappear, or have peak amplitudes, the characteristic shape and location of the bow shock can be inferred (cf. *Fuselier et al.*'s [1986] analysis using electron data). Thus, by studying variations in the plasma wave and magnetic field data one can perform a "remote-sensing" analysis of the characteristics of a planet's bow shock. Here we use this technique to remotely infer the existence of large-scale changes in the position and perhaps the shape of Neptune's bow shock prior to Voyager 2's inbound crossing of the bow shock. In different time periods these changes are separately interpreted in terms of rotation of Neptune's tilted magnetic dipole and solar wind ram pressure variations.

Belcher et al. [1989] and *Ness et al.* [1989] have suggested that the rotation of Neptune's oblique, tilted magnetic field should produce periodic changes in the structure of Neptune's magnetosphere and magnetopause. Theoretical modeling of this situation confirms these periodic changes in magnetospheric structure [*Voigt and Ness*, 1990]. It is possible that variations in the location and/or shape of the bow shock might accompany these changes in magnetospheric structure. The results of the analyses in this paper suggest that rotational control of Neptune's bow shock, and so the magnetosphere as a whole, does indeed occur. The bow shock positions and shapes derived in this paper should enable testing of future theoretical models attempting to

[1]Department of Physics and Astronomy, University of Iowa, Iowa City.
[2]Bartol Research Institute, University of Delaware, Newark.
[3]TRW Space and Technology Group, Redondo Beach, California.

Copyright 1991 by the American Geophysical Union.

Paper number 91JA01929.
0148-0227/91/91JA-01929$05.00

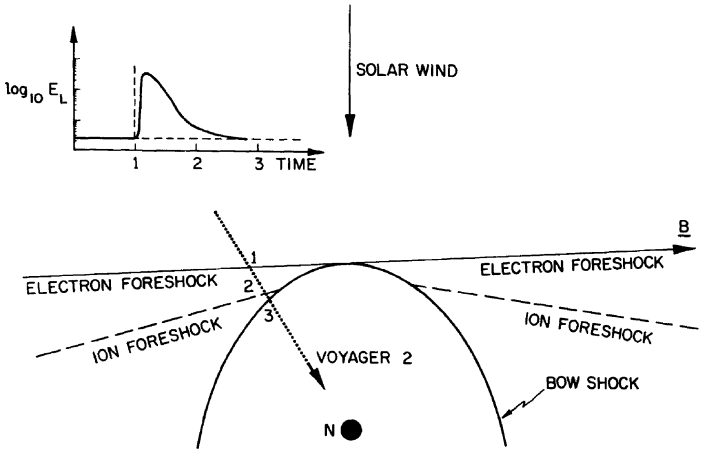

Fig. 1. The expected structure of Neptune's foreshock, showing the tangent magnetic field line, the electron and ion foreshocks, and the bow shock. The expected time history of the Langmuir electric field E_L along the (dotted) spacecraft trajectory is also shown.

describe time variations in the location of Neptune's bow shock.

The framework of this paper is as follows. Section 2 contains an explanation of the theoretical concepts and procedures used in the remote-sensing analysis. The plasma wave data are presented and discussed in section 3, after which the magnetic field data are presented in section 4. Section 5 presents the variations in the position and shape of Neptune's bow shock inferred from the remote-sensing analysis. Voyager 2's trajectory relative to the inferred tangent points and shock locations is described in section 6. In section 7 we separate the large-scale motions of the bow shock into motions caused by variations in the solar wind ram pressure and variations caused by rotational changes in the orientation of Neptune's magnetic dipole relative to the solar direction. The results of the paper are discussed in section 8, and the conclusions are given in section 9.

2. The Remote-Sensing Analysis: Theoretical Concepts and Background

Figure 1 illustrates the amplitude of electron plasma waves expected when a spacecraft enters a planetary foreshock along the trajectory indicated. Energetic electrons streaming away from the shock, and the associated Langmuir waves, are constrained to lie downstream from the magnetic field line tangent to the bow shock. This region is called the electron foreshock [e.g., *Klimas*, 1985]. Changes in the magnetic field direction, the shape and location of the bow shock, and the spacecraft's motion can cause the foreshock's streaming electrons and associated Langmuir waves to sweep over the spacecraft, resulting in the appearance and disappearance of the waves.

If the solar wind speed relative to the electron streaming speed is neglected, the spacecraft position and magnetic field direction corresponding to the onset or disappearance of the waves at the upstream edge of the foreshock define the magnetic field line connecting the spacecraft to the tangent point on the bow shock. A natural Neptune-centered coordinate system analogous to the GSE system is used: the X axis points sunward from the planet, the Y axis lies approximately antiparallel to Neptune's orbital velocity in the orbital plane, and the Z axis completes a right-handed coordinate system. The equation of a magnetic field line with orientation (B_X, B_Y, B_Z) passing through the spacecraft position (X_{sc}, Y_{sc}, Z_{sc}) is

$$\frac{X - X_{sc}}{B_X} = \frac{Y - Y_{sc}}{B_Y} = \frac{Z - Z_{sc}}{B_Z} = t. \quad (1)$$

Straight magnetic field lines are assumed. Curvature effects due to the Parker spiral and magnetic turbulence are estimated in section 5. These effects are found to be small sources of error for the remote-sensing analysis. The bow shock is represented by the paraboloid

$$X = a_s - b_s(Y^2 + Z^2) \quad (2)$$

where the parameter a_s is the nose position (or standoff distance) of the shock and the parameter b_s is related to the flaring of the shock. Aberration of the bow shock due to Neptune's orbital motion is of the order of 0.7° and is neglected here. The possibility that the shock's symmetry axis does not lie along the X axis is discussed in section 8. Choice of a paraboloid shock shape, rather than a hyperboloid for example, is justified by (1) the fact that the tangent points found in this paper are all near the nose of the shock where the paraboloidal description is more appropriate, (2) algebraic simplicity, and (3) convention in connection analyses [i.e., *Filbert and Kellogg*, 1979; *Fuselier et al.*, 1986]. Discussion of the symmetry of the shock surface is deferred to section 8. The parameter b_s is related to the transverse distance $\rho_0 = (Y^2 + Z^2)^{1/2}$ of the shock from the Sun-Neptune line at $X = 0$ by $\rho_0 = (a_s/b_s)^{1/2}$.

Constraints on the shock parameters a_s and b_s follow on considering the conditions for magnetic connection of the spacecraft to the tangent point. Equation (1) is rewritten as three separate expressions for X, Y, and Z as a function of the t parameter, the magnetic field components, and the spacecraft position. A quadratic equation for t is obtained by

substituting these expressions into equation (2) and rearranging. We note that connection of the spacecraft to the tangent point corresponds to this quadratic equation having only one real solution; the constraints on the tangent point follow from the quadratic determinant being zero. This procedure gives two results. The first is a relation between the a_s and b_s parameters of the shock in terms of the magnetic field components and the spacecraft position:

$$X_{sc} = a_s + \frac{B_X^2}{4b_s\alpha} + \frac{\beta B_X}{\alpha} + \frac{\beta^2 b_s}{\alpha} - \gamma b_s \qquad (3)$$

Here $\alpha = B_Y^2 + B_Z^2$, $\beta = B_Y Y_{sc} + B_Z Z_{sc}$, and $\gamma = Y_{sc}^2 + Z_{sc}^2$. Notice that a_s and b_s cannot be determined uniquely by this procedure from the spacecraft position and magnetic field direction for one foreshock crossing. However, values for a_s and b_s can be determined uniquely if the tangent line is crossed twice (with the shock remaining stationary) by solving the two versions of (3) simultaneously. This technique is termed the "pairwise" analysis hereafter. Alternatively, best fit or least squares techniques can be used in the overdetermined case where more than two sets of magnetic field vectors and spacecraft locations are identified with crossings of the foreshock boundary. The second result specifies the t parameter, and so the location, of the tangent point:

$$t = -\frac{(B_X/b_s) + 2\beta}{2\alpha}. \qquad (4)$$

Once the parameter b_s is known, the location of the tangent point can be calculated using (1) and (4).

In practice the idealized procedure described above may encounter difficulties in adequately identifying the times of foreshock entrances and exits for the remote-sensing analysis. These difficulties include low time resolution data, spacecraft interference signals, instrumental backgrounds significant compared with the wave levels of the most nearly tangent magnetic field lines (e.g., compare Figures 1 and 2), and multiple foreshock encounters in close succession that may not be time-resolvable. Unfortunately, these problems are all relevant to the analysis of the Neptune foreshock data. In addition, the remote-sensing analysis assumes that large-scale changes in the magnetic field direction cause the foreshock to sweep back and forth across the spacecraft. Local fluctuations in the magnetic field direction must therefore be minimized, and care must be taken that changes in the field direction last at least as long as representative travel times from the shock to the spacecraft. Electrons with speeds 10^7–10^8 m s^{-1} travel distances of 1–10 R_N in times of 0.25–25 s. All the above difficulties are minimized and the requirements addressed by choosing relatively stable, long-lived (at least 8 s, but ideally longer than 25 s) wave events for analysis. This permits time averaging of the magnetic field data and rejection of deviant data points. In addition, as described in the next section, the definitions of wave events identified with magnetic connection to the tangent point are broadened and refined.

3. PLASMA WAVE DATA

The characteristics of the Voyager plasma wave instrument are described by *Scarf and Gurnett* [1977]. Here we are concerned only with electric field data from the 16-channel spectrum analyzer system; no wideband frames were taken while Voyager 2 moved through Neptune's foreshock. A complete plasma wave spectrum from 10 Hz to 56.2 kHz is available every 4 s. Overviews of the plasma waves detected during the Neptune encounter are given by *Gurnett et al.* [1989]. Figure 2*a* shows a 20-s time-averaged history of all the Langmuir waves observed in Neptune's foreshock. Langmuir waves were observed from 1040 to 1440 SCET, day 236, 1989, during the inbound pass. No Langmuir waves have presently been identified in the outbound foreshock data. The figure shows that the waves were confined to the 562-Hz channel except for a few spiky events in the 1-kHz and 311-Hz channels. The waves occurred during two periods, 1040–1115 SCET and 1240–1440 SCET, with an intervening 85-min period without observable waves. Two vertical dashed lines identify the period of the inbound bow shock crossing, 1435–1448 SCET, according to the plasma wave data (*Moses et al.* [1990] discuss this period in detail). The level of Langmuir waves decreases to zero as the spacecraft moves closer to and into the shock and downstream region. During the two observation periods many distinct wave events occur, often with several peaks per event. This is true for both the well-separated wave events observed from 1040 to 1115 SCET and the more continuous wave events from 1255 to 1440 SCET. The presence of many time-separated events in the Langmuir wave data (including stable maxima, deep nulls, and brief periods of background wave levels) indicates that Voyager entered and left the foreshock many times, thereby permitting multiple determinations of the shock parameters a_s and b_s over a time period of approximately 4 hours. Correlations of the plasma wave and magnetic field data (section 4) do indeed confirm that most events in the wave data are definitely associated with changes in the magnetic field direction, and so the connection geometry of the spacecraft.

The timing and nature of the wave events, particularly peaks in the wave amplitude, are best identified in Figure 2*b*, where no time averaging is performed. Some care must be taken in interpreting the PWS data because of the presence of regular spacecraft interference signals and irregularly occurring thruster firings. Interference signals can be separated from Langmuir wave events and thruster firings by their periodicity in time, duration, and amplitude. For instance, the signals from 1030 to 1039 SCET are all interference signals. In contrast, the event near 1040:35 SCET is either a Langmuir wave signal or a thruster firing since it occurs during a periodic null of the interference signals (and has a larger amplitude and different time history). Langmuir wave events can therefore generally be separated from interference signals without great difficulty. However, detailed timing information for thruster firings is not available. In the PWS data, thruster firings are seen as impulsive signals that often extend into neighboring channels and are more intense at lower frequencies. Thus wave events localized in the 562-Hz channel and lasting more than 4 s are most unlikely to be thruster firings. The absence of correlated spikes in neighboring channels for the 1040–1115 SCET events (see Figure 2*a*) indicates that thruster firings do not produce the observed signals. Events in the period 1241–1449 SCET are not analyzed further because they appear in more than one channel and occur in conjunction with bad magnetic field data, thereby most likely being telemetry

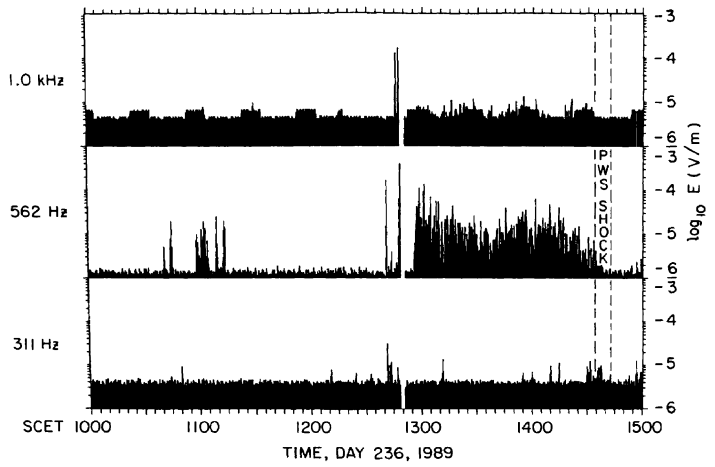

Fig. 2*a*. Voyager plasma wave data showing all the Langmuir waves observed inbound to Neptune. These data are averaged over 20 s. The waves, primarily in the 562-Hz channel, occur in many bursts arranged in two main periods separated by 85 min. The existence of onsets and disappearances of the waves implies multiple entries into and exist from the foreshock.

errors. The small number of impulsive signals in the 311-Hz and 1-kHz channels for the period 1255–1440 SCET indicates that only a few thruster firings occurred, leading to at most a few thruster events being misidentified as wave events during this interval.

Intrinsic time variations in wave levels while stably connected in the foreshock, corresponding to well-defined wave packets for example, could conceivably be misidentified as connection/disconnection events with resulting implications for the remote-sensing analysis. It is likely, on the basis of direct observations at Jupiter [*Gurnett et al.*, 1981*b*] and indirect observations at Earth [*Anderson et al.*, 1981; *Etcheto and Faucheux*, 1984; *Fuselier et al.*, 1985; *Lacombe et al.*, 1985], that the Langmuir waves in Neptune's foreshock

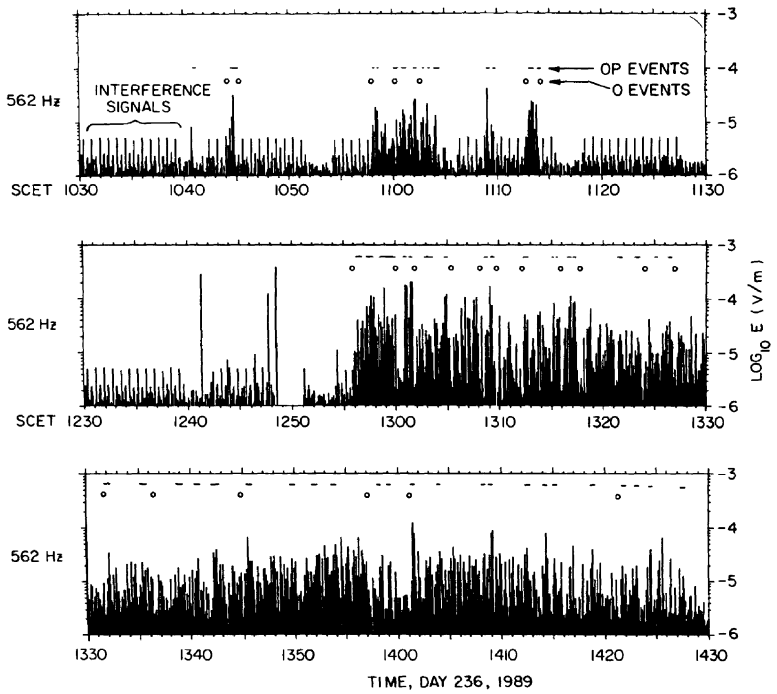

Fig. 2*b*. Detailed, unaveraged, 562-Hz channel data. All the OP and O events analyzed are shown with dashes and open circles, respectively.

sometimes occur in well-defined wave packets with time scales of the order of a few hundred milliseconds or less. In comparison, the PWS receiver reports the logarithm of the electric field in each channel with a 50-ms averaging time constant, sampled every 4 s. Closely time-separated wave packets with comparable amplitudes should be accurately sampled by the detector. Only when the wave packets have very different amplitudes or are well separated in time is the detector expected to show great variability between successive data points or to greatly underestimate the electric fields present in the plasma. Wave packet effects are therefore eliminated here by considering only relatively long lived, stable wave events and by requiring wave events to have associated magnetic signatures.

We distinguish two classes of wave events for analysis. The primary class analyzed, termed on-peak events and given the symbol "OP," is intended to correspond directly with the maximum in the Langmuir wave amplitude expected near the upstream edge of the foreshock (e.g., Figure 1). Observationally, OP events are defined as time-localized, relatively long lived events with relatively stable high wave levels that include a maximum or several maxima in the wave amplitude. OP events are required to last longer than 2 PWS samples (8 s) so as to avoid contamination with wave packet effects, to allow electron propagation from the shock to the spacecraft along large-scale straight magnetic field lines, and to permit significant time averaging of the magnetic field data. Almost all OP events analyzed here last longer than 12 s, with several events lasting longer than 1 min. The dashes in Figure 2*b* show the times of all OP events analyzed. The second class of wave events analyzed, termed on/off events and given the symbol "O," is intended to correspond with entrances into and exits from the upstream portion of the foreshock (see Figure 1). Observationally, these events involve the wave amplitude varying from below the background level toward the high levels of OP events. Magnetic field data are used to eliminate events in which the low wave levels correspond to the spacecraft being downstream from the peak wave levels (i.e., near the ion foreshock in Figure 1). Open circles in Figure 2*b* show the times of all O events analyzed here. These events are all relatively slow foreshock transitions that last longer than 8 s so as to permit significant averaging of the magnetic field data. Peaks lasting for only one data sample are not analyzed individually because of possible confusion with wave packet effects, thruster firings, and local magnetic field variations. As defined above, these two classes of events have somewhat different interpretations in terms of position in the foreshock (see Figure 1). Despite these differences, we find empirically that analyses of these two classes of events leads to shock parameters a_s and b_s that are consistent.

Observational and theoretical justifications for considering these two classes of wave events are now explored. Regarding OP events, it is well known that the highest Langmuir wave levels are observed near the upstream edge of Earth's foreshock [*Filbert and Kellogg*, 1979; *Etcheto and Faucheux*, 1984; *Gurnett*, 1985, Figure 11]. Accordingly, by analogy, the observation of a well-defined peak in the wave data can be taken as evidence for the spacecraft being very near the upstream edge of Neptune's foreshock. Ideally, confirmation of this identification should be possible from the magnetometer data: time variations in the magnetic field data should coincide with the wave event and be qualitatively suitable for positioning the spacecraft near the upstream boundary of the foreshock. At Neptune we found that essentially all the OP events analyzed had appropriate magnetic signatures. In addition, the region of Neptune's foreshock with significant wave levels is expected theoretically (see appendix) to have an angular width less than 10°. Since the region with peak wave levels will have a significantly smaller size and be found close to the foreshock boundary, identifying this region with the tangent field line is not expected to introduce significant errors. From a practical viewpoint, OP events are not easily subject to misidentification, because they are times of long-lived enhanced wave levels. The above points justify our analysis of OP events. O events are directly associated with the upstream boundary of the foreshock, thereby requiring no further theoretical justification. Observationally, however, O events are more easily subject to misidentification than OP events. For instance, the timing of an O event is somewhat subjective in that the event involves wave levels varying from below the instrumental background level to high levels. Attention was therefore restricted to O events with slow boundary crossings for which a smooth progression in wave amplitude occurred.

Krimigis et al. [1989] state that the low-energy charged particle (LECP) data do not show clear evidence for upstream enhancements of bow shock–associated energetic electrons and ions. The presence of the Langmuir waves is, however, clear evidence for the existence of an electron foreshock and energetic upstream electrons; the large threshold energy for the LECP's electron detectors (22 keV, corresponding to 200 thermal speeds) is probably the reason for the lack of observed energetic electrons. Given that the Langmuir wave data imply multiple entries into and exits from the electron foreshock, it is natural to inquire whether the plasma wave data show any evidence of entry into an ion foreshock region. Searches of the PWS data for lower-frequency electrostatic waves interpretable as ion acoustic waves driven by streaming ions in an ion foreshock, analogous to those observed in the ion foreshocks of Earth [i.e., *Anderson et al.*, 1981; *Gurnett*, 1985; *Thomsen*, 1985] and Jupiter [*Scarf et al.* 1979], have not met with success to date. Consistent with this result, section 6 shows that the magnetic field direction and spacecraft trajectory are not favorable for Voyager to enter the ion foreshock inbound to Neptune.

4. MAGNETIC FIELD DATA

Behannon et al. [1977] describe the magnetic field instrument on the Voyager 2 spacecraft. The data presented here are 1.92-s averages of the 60-ms vector field measurements from Voyager 2's inboard magnetometer, courtesy of N. F. Ness and R. P. Lepping. Data from the outboard magnetometer are unusable at this time because of interference. The inboard magnetometer data have been corrected for spacecraft fields using offsets calculated by R. P. Lepping. For the Neptune encounter the magnetic field data may be transferred from the usual (R, T, N) solar equatorial system to the Neptune-centered system defined in section 2 by changing the sign of the R and T components: $(B_X, B_Y, B_Z) = (-B_R, -B_T, B_N)$. This procedure should be accurate to within a few percent in each component.

Figure 3 shows the magnetic field components B_X, B_Y, and B_Z for the period 1000–1400 SCET, day 236, 1989, together with the plasma wave data from the 562-Hz channel. The

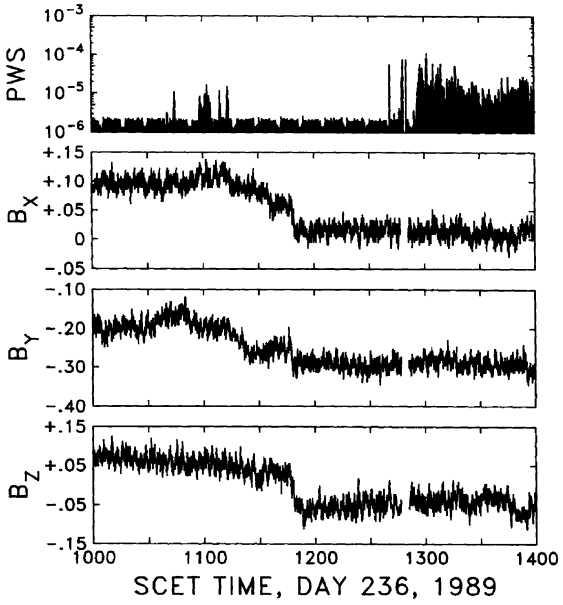

Fig. 3. The three bottom panels show the B_X, B_Y, and B_Z components of the magnetic field (in nanoteslas) for the time period 1000–1400 SCET, day 236, 1989. The top panel shows the 562-Hz PWS data on the same time scale. Detailed inspection shows that almost all long-lived wave events are correlated with changes in the magnetic field direction. The large-scale rotation of the field from 1115 to 1200 SCET disconnects Voyager from the shock.

magnetic field is observed to be relatively stable during each half of the 4-hour period but exhibits a large rotation that begins at approximately 1115 SCET and ends shortly before 1200 SCET. After this rotation the magnetic field lies almost entirely along the $-Y$ axis. This field orientation leads to connection phenomena being relatively insensitive to the shock parameter b_s but very sensitive to the standoff distance a_s (see equation (3) with $B_Y = B_T$ and $Z_{sc} \sim 0$). Accordingly, as shown below, the remote-sensing analysis determines the shock's a_s parameter well but the b_s parameter poorly for the wave events after 1255 SCET. Prior to the rotation the angle in the X-Y plane between the X axis and the magnetic field is approximately $-60°$, but after the rotation it is approximately $-85°$ as expected on the basis of the Parker spiral model. Similarly, the angle between the X axis and the magnetic field in the X-Z plane varies from approximately $+35°$ to $-70°$ before and after the rotation, respectively. The large rotation of the field between 1115 and 1200 SCET is clearly a likely cause for the spacecraft being disconnected from the shock surface as evidenced by the lack of plasma waves from 1115 to 1240 SCET. In section 7 we show that the solar wind ram pressure also increases by a factor of 3 during this time period, thereby being another cause for disconnection of the spacecraft from the shock. The resumption of wave activity near 1240 SCET with the new field configuration indicates renewed connection to the shock.

Comparing the plasma wave data with the magnetic field data permits one to qualitatively test whether the on/off and peak wave events are associated with changes in the magnetic field direction. Positive changes in the B_X and B_Y components correspond to the magnetic field vector pointing more toward the Sun, and so to sunward movement of the foreshock. Several wave events that are clearly correlated with changes in the field can be seen in Figure 3. Many wave events are associated with magnetic field changes that are too subtle to be seen on the scale used in Figure 3. Close inspection of these events almost invariably shows that small variations of the magnetic field consistent with a change in magnetic connection do occur at these times. However, as discussed below, the magnetic field data are contaminated with spacecraft interference signals. It appears that these interference signals sometimes disguise the field variations corresponding to a wave event and at other times suggest that a wave event should have occurred where none was observed. In summary, the magnetic field data imply that most wave events are definitely associated with magnetic connection and disconnection from the bow shock.

The analysis of connection events evident in the plasma wave data is complicated by the presence of high levels of interference signals in the magnetic field data. These interference signals are similar to those discussed extensively by *Russell et al.* [1990] for the Uranus encounter. Figure 4 shows the diagonal elements of the spectral density matrix for the magnetic field data from 1000 to 1400 SCET, day 236. These power spectra are very similar to those calculated for a similar data interval 1 week earlier (day 229, August 17, 1989). Strong interference is immediately apparent at 3.9 mHz (256-s period), 5.2 mHz (192 s), and 6.5 mHz (154 s), with either higher harmonics or leaked power evident at higher frequencies. These signals correspond to harmonics of a 768-s pure tone and are believed to be associated with operation of the spacecraft. The fundamental pure tone is evident in spectra computed for longer periods of time. All noise signals shown in the figure are pure tones or leaked power. The frequency breadth of each harmonic signal in Figure 4, ideally a pure tone, is determined by the smoothing

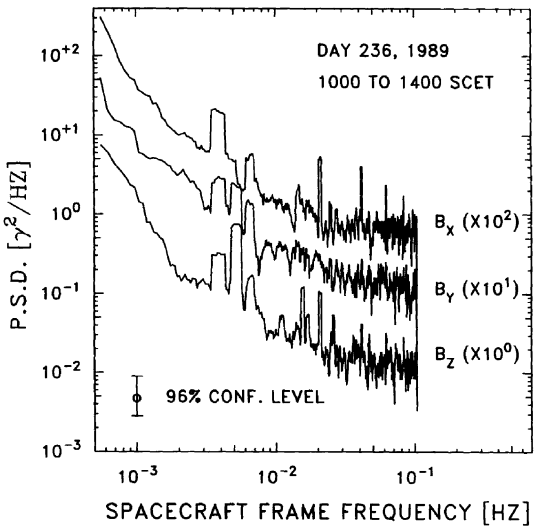

Fig. 4. Power spectra for the B_X, B_Y, and B_Z components from 1000 to 1400 SCET, showing the presence of spacecraft interference signals at frequencies up to and above 0.1 Hz.

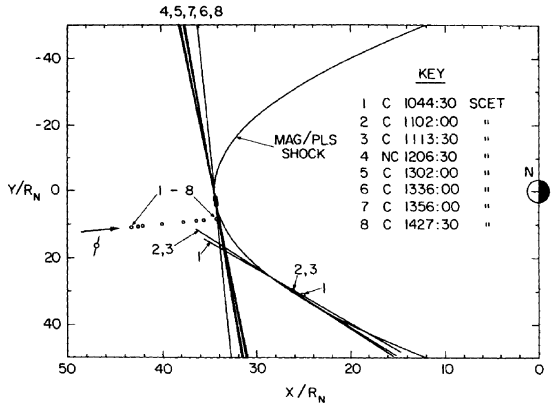

Fig. 5. First evidence for large-scale motions of Neptune's bow shock. Numbers 1–8 denote the spacecraft locations and tangent magnetic field lines at times given in the key. The shock shown is the MAG/PLS model described in the text. Magnetic connection to the shock at times 1–3 and 5–8, as required to explain the observed wave events, requires the shock to be located near 38–41 R_N. The finite thickness of the foreshock requires continual planetward motion of the shock after 1300 SCET. These results are inconsistent with the static MAG and PLS shock models.

required to provide statistical weight to the physically significant spectral elements. The spectra shown were smoothed over 13 adjacent spectral estimates to provide a statistical weight of 26. The associated 96% confidence level is shown in the figure. All components of the measured magnetic field vector are affected by the interference.

The presence of strong interference signals in the magnetic field data at frequencies up to 0.1 Hz, near the sampling rate of 0.52 Hz for the data used here, means that individual magnetic field data points cannot be trusted implicitly. Unfortunately, the data cannot be filtered to remove the interference signals since the connection analysis depends sensitively on the magnetic field direction (and so the phase of the unfiltered signal). Attempts to identify the interference signals in the time series data have not met with success to date. The interference is minimized here by using time averages of the magnetic field directions for relatively long lived OP and O events. In addition, we note that the timing of the wave events shows no noticeable periodicity. Accordingly, since the remote-sensing analyses below show a consistent picture for the location and motion of Neptune's bow shock, we contend that the presence of noise in the magnetometer (MAG) data is not a significant source of error.

5. SHOCK CHARACTERISTICS GIVEN BY REMOTE-SENSING ANALYSES

5.1. *Preliminary Analyses*

Strong evidence for large-scale motions of Neptune's bow shock can be obtained without performing a complete remote-sensing analysis. The simplest analysis demonstrating the necessity for large-scale shock motions is shown in Figure 5. The points labeled 1–8 show the position of the Voyager spacecraft projected into the X-Y plane at times given in the key ($|Z_{SC}| < 0.4\ R_N$ from 1040 to 1430 SCET). Time periods during which Langmuir waves were observed, and so the spacecraft was magnetically connected to the shock, are labeled with a C in the key. The label NC for the period centered at 1206:30 SCET means that the spacecraft was not magnetically connected to the shock at this time. Lines 1–8 show the tangent magnetic field lines, averaged appropriately, at times 1–8 for a shock model given by the *Belcher et al.* [1989] and *Ness et al.* [1989] observations. Averages were performed over periods of 40 s and 2 min for period 1 and periods 2–8, respectively. The position of the tangent point for each period is calculated using the magnetic field direction, a shock model, and standard foreshock theory [*Cairns*, 1987*a*; *Fitzenreiter et al.*, 1990, Appendix A]. Squares show the location of the tangent point for each time. Models for Neptune's bow shock based on the inbound and outbound shock crossings are given by *Belcher et al.* [1989, Figure 2] and *Ness et al.* [1989, Figure 2]. For $X \geq 0$ these authors' hyperboloidal shock shapes are closely approximated by paraboloids. The Belcher et al. model, termed the PLS model here, has $a_s \sim 34.7\ R_N$ (M. Zhang, personal communication, 1991) and $b_s \sim 0.010\ R_N^{-1}$. The Ness et al. model, termed the MAG model, has $a_s \sim 34.2\ R_N$ and $b_s \sim 0.008\ R_N^{-1}$. The shock model in Figure 5, termed the MAG/PLS model, has $a_s = 34.45\ R_N$ and $b_s = 0.009\ R_N^{-1}$.

Figure 5 demonstrates the following results. (1) The spacecraft locations and magnetic field directions for the observed wave events prior to about 1427 SCET are inconsistent with the static MAG/PLS, MAG, and PLS shock models. Instead, the plasma wave and magnetic field data require that large-scale motions of Neptune's bow shock occur. (2) Assuming that the shock has b_s in the range 0.008–0.01 R_N^{-1} of the MAG and PLS models, the shock's nose has to be located near 38 R_N to explain the 1040–1115 SCET wave events. (3) The onset of wave events after 1300 SCET, coupled with the magnetic field lying almost entirely along the $-Y$ axis after this time, requires that the shock's standoff distance a_s is of the order of 38.5 R_N near 1300 SCET almost irrespective of the value of b_s. (4) The X thickness of the foreshock region containing high levels of Langmuir waves should have been significantly less than 0.5 R_N after about 1115 SCET. Voyager would have crossed such a static foreshock region in less than 15 min. (5) The continual presence of Langmuir waves from 1255 to 1430 SCET, despite the finite foreshock size, requires that the bow shock move continuously planetward after 1300 SCET. (6) Voyager's disconnection from the shock after 1115 SCET can be understood in terms of the observed magnetic field rotation.

A partial remote-sensing analysis can be used to set conservative limits on the location and motion of the shock. Equation (3) can be solved directly for a_s as a function of time if a constant value of b_s is assumed and average magnetic field vectors and spacecraft locations for periods of high wave activity are specified. Figure 6 shows the results of this procedure for b_s in the range of the MAG and PLS shock models and 2-min-averaged magnetic field vectors (the averaging intervals for the 1040:43 and 1044:30 events are 10 s and 40 s, respectively). As expected, the figure explicitly shows results 1–3 and 5 above. In particular, the shock had a_s in the range 37–41 R_N (with weak evidence for a peak in a_s) from 1040 to 1115 SCET. Furthermore, the shock moved monotonically planetward from 1300 to 1430 SCET with $a_s \sim 38.5\ R_N$ near 1300 SCET. Note, moreover, that small

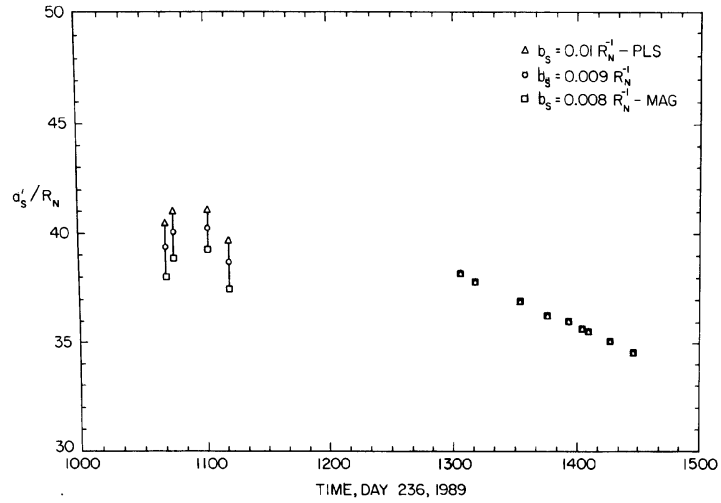

Fig. 6. Conservative remote-sensing analysis in which b_s is required to lie in the range of the MAG and PLS shock models. Averaged magnetic field directions and spacecraft locations for particular wave events then lead to the plotted ranges for a_s'. Standoff distances near 38–41 R_N for the first wave period and a continuous decrease from 38.5 to 34.2 R_N during the second wave period are clearly visible. These results are consistent with Figure 5.

differences in b_s can lead to considerable scatter in a_s for the 1400–1115 SCET events but very little scatter for the events after 1300. The lack of scatter for events after 1300 SCET is due to the magnetic field being directed in the $-Y$ direction ($B_Y/B \sim -0.99$): this requires $a_s \sim X_{sc}$ irrespective of b_s (i.e., $B_X \sim B_Z = 0$ in equation (3)). The distance between the spacecraft and the tangent point on the shock can be calculated using standard foreshock theory [*Cairns*, 1987*a*; *Fitzenreiter et al.*, 1990, Appendix A], the above shock parameters, and the magnetic field directions during the wave events. We find that Voyager was located approximately 20 and 5 R_N from the (moving) tangent point during the periods 1040–1115 and 1255–1430 SCET, respectively. The long electron transit times for the period 1040–1115 SCET (see section 2) suggest that further time averaging of these data is advisable. Accordingly, neighboring OP events during this period were combined for the complete remote-sensing analysis described next. This led to eight averaged OP events that each lasted more than 20 s (except for the 1040 SCET event) instead of the original 15 OP events.

5.2. *The Complete Remote-Sensing Analysis*

Average magnetic field vectors and spacecraft locations were calculated for each OP or O event in Figure 2*b* by averaging over the period of the wave event (taking into account time offsets between the PWS and MAG data) and rejecting any clearly deviant data points. We used two techniques for remotely sensing the time-varying a_s and b_s parameters of the shock: the "pairwise" analysis (see section 2), in which the two versions of equation (3) for a pair of wave events are solved simultaneously, and a least squares analysis permitting time variations in a_s and b_s.

Careful consideration of the pairwise technique suggests that it is generally best suited to analyzing data for which the shock characteristics vary slowly and the spacecraft locations and magnetic field directions differ significantly between wave events. Analyses of wave events too closely separated in time (and position) are likely to be problematic since the expected small differences in large-scale magnetic field direction may be swamped by local fluctuations and noise in the magnetic field data. Similarly, as described below, event separations during which the shock moves significantly will lead to biased results. Noting that Voyager moves approximately 0.2 R_N every 5 min and that Figures 5 and 6 demonstrate that the shock moves significantly, we primarily analyze pairs of wave events with time separations between 3 min and 30 min. Subject to these time restrictions, a single wave event can be used in multiple determinations of the shock parameters. In addition to these pairs of events, however, we note that the pairwise technique is almost ideally suited to analyzing pairs of events with one event from each of the two wave periods. This is due to the significant differences in spacecraft position and magnetic field direction, yet similar shock locations (Figures 5 and 6), for these events. Accordingly, all pairs of wave events with one member from each of the periods 1040–1115 and 1255–1315 SCET are also analyzed. Figures 7 and 8 show the time variations in the a_s and b_s parameters of the shock resulting from the analysis of pairs of OP events, subject to the above restrictions. Each small circle shows the a_s or b_s parameter at the central time of a pair of OP events. Solid triangles show the results of calculations with time-sequential OP events (subject to the 3-min minimum time separation). Squares show the results of the pairwise analysis for the time-averaged data used in Figure 6. The times of the individual OP events are shown by plus signs near $a_s = 30$ R_N and $b_s = 0.03\ R_N^{-1}$ in Figures 7 and 8, respectively. Finally, the a_s and b_s parameters of the MAG and PLS models are shown by arrows in both figures.

The results of the complete remote-sensing analysis confirm the results of the earlier analyses, as well as providing important information on the b_s parameter of Neptune's

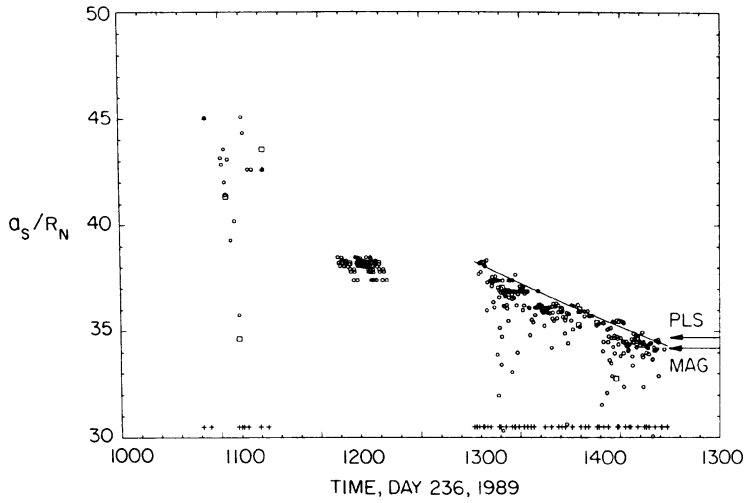

Fig. 7. Time history of the a_s parameters determined by the complete "pairwise" remote-sensing analysis for the OP events (circles). The results of time-sequential pairs of OP events and pairs of the average wave events used in Figure 6 are shown using triangles and squares, respectively. The times of individual OP events are shown using plus signs. During the first wave period the a_s values are scattered in the range 39–45 R_N with an average near 42.3 R_N. The second wave period shows a continual decrease from 38.5 R_N to 34 R_N (together with scattered lower values). The inbound shock crossing occurred at $X \sim 34.0$ R_N. This is consistent with the extrapolated a_s values given by the remote-sensing analysis and the a_s parameters of the MAG and PLS models (arrows).

shock. (1) The static MAG and PLS shock models are not consistent with the plasma wave and magnetic field data. Instead, these data require that large-scale motions of the shock occur. (2) Combining wave events from the periods 1040–1115 SCET and 1255–1315 SCET in pairs leads to the cluster of shock parameters near 1200 SCET: $a_s \sim 38.2 \pm 0.6$ R_N and $b_s \sim 0.008 \pm 0.002$ R_N^{-1}. This value for b_s agrees very well with the MAG and PLS shock models, particularly the MAG model. As noted above, the remote-sensing analysis is almost ideally suited to analyzing these pairs of events. These results, as well as confirming that the average value of b_s for Neptune's bow shock is approximately 0.008

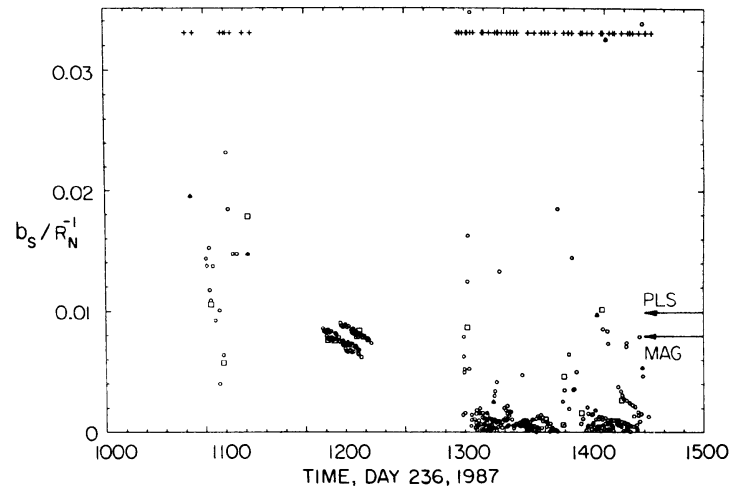

Fig. 8. Time history of the b_s parameters determined by the remote-sensing analysis in the same format as Figure 7. The cluster of points near 1200 SCET, resulting from pairs of wave events best suited to the remote-sensing analysis, gives a best estimate for b_s: 0.008 ± 0.002 R_N^{-1}. This value agrees very well with the MAG and PLS models (arrows). During the first wave period the b_s values are scattered primarily in the range 0.008–0.02 R_N^{-1} with an average of 0.014 R_N^{-1}. The second wave period shows a definite bias toward unrealistically low values for b_s (<0.002 R_N^{-1}). This bias is interpreted in the text in terms of shock motions. The 10% of points with $b_s > 0.002$ R_N^{-1} have an average value of the order of 0.008 R_N^{-1}, consistent with the best estimate above. The values $b_s = 0.014$ R_N^{-1} and 0.008 R_N^{-1} are used hereafter for the first and second wave periods.

R_N^{-1}, argue that the remote-sensing analysis is working well. (3) The wave events from 1040 to 1115 SCET are consistent with the shock having average parameters $a_s = 42.3 \pm 2\ R_N$ and $b_s = 0.014 \pm 0.01\ R_N^{-1}$ during this period. No consistent trend in the shock's motion is evident. (4) The shock moves continuously planetward during the interval 1255–1430 SCET, starting with $a_s \sim 38.3\ R_N$ near 1300 SCET. The b_s points show a clear bias toward unrealistically low values; however, approximately 10% of the values are within a factor of 2 of the average value $b_s \sim 0.008\ R_N^{-1}$ determined above. This bias is interpreted below as an effect of the shock's motion and the magnetic field being almost perpendicular to the X direction. (5) The remotely sensed shock parameters are consistent with the time and location of Voyager's inbound shock crossing. (6) Analyses of the OP events, O events (not shown), and average wave events all show qualitatively and quantitatively similar results. (7) The shock speed inferred for the period 1255–1430 SCET is commensurate with the spacecraft's speed, as required to explain the duration of this foreshock encounter.

The data were also analyzed using a least squares technique in which the trial functions are versions of equation (3) with various orders and combinations of the Taylor-expanded a_s and b_s parameters retained. The solid curve in Figure 7 shows the results of a three-parameter fit to all the OP events after 1255 SCET. In this case, with 1340 SCET being the central time t_c, $a_s(t_c) = 36.2\ R_N$, $a_s' = \partial a_s/\partial t \sim -0.00067\ R_N\ s^{-1} \sim 17$ km s^{-1}, and $b_s(t_c) = 0.0031\ R_N^{-1}$. Very similar histories for $a_s(t)$ result when b_s is assumed to have a constant value in the range 0.008–0.01 R_N^{-1}, when all first and second time derivatives are included, and when the data interval is varied. This is due to the remote-sensing analysis being very insensitive to the shock's b_s parameter when $B_Y \sim -B$.

The magnetic field orientation during the period 1255–1430 SCET, magnetic field turbulence, interference signals in the magnetic field data, and shock motions on time scales similar to the time separation of two wave events can potentially affect the results of the pairwise and least squares versions of the remote-sensing analysis. In particular, these effects can lead to there being no solution to the two versions of (3) for a pair of wave events. Indications that these effects do affect the pairwise analysis is provided by the following: out of 1596 pairs of events obeying the time restrictions above, only 537 pairs had solutions. Happily, a high proportion (363 out of 537) of these solutions were acceptable, i.e., $a_s, b_s > 0$ and $b_s < 0.05\ R_N^{-1}$. In addition, the combination of shock motions and the magnetic field being almost perpendicular to the Sun-Neptune direction can lead to a natural bias for blunt shock solutions with very small values for b_s. This bias arises because the shock's a_s parameter is determined almost entirely by the most planetward observation, and the b_s parameter must therefore be very small (i.e., a blunt shock) if the difference in magnetic field direction between the two observation points is small. This is our interpretation for the bias toward very small values of b_s in analysis of data from the period 1255–1430 SCET (when the shock was moving planetward). The value $b_s = 0.008\ R_N^{-1}$, equal to the best estimate derived above for the remote-sensing analysis and to the value for the MAG model, is therefore assigned to the shock for this period since this motion/orientation bias is evidently dominant for this data set. (This bias does not affect the a_s values determined for this period because of the favorable magnetic field orientation; see equation (3) and Figure 6.) Sunward motion of the shock can bias the analysis to larger values of b_s (and so a_s) than are correct. This may be relevant to the wave events from 1040 to 1115 SCET. However, the absence of any clear trend in a_s for these events renders this interpretation problematical. We regard Figure 7 as providing weak evidence that the shock's b_s parameter is larger than 0.008–0.01 R_N^{-1} during the period 1040–1115 SCET.

Magnetic field line curvature and interference signals, in addition to the effects of field line orientation and shock motion just described, may cause some of the scatter in Figures 7 and 8. The Parker spiral and magnetic field turbulence are the two primary sources of field curvature. (This magnetic turbulence is primarily of solar wind origin since Voyager most probably did not enter the ion foreshock.) Connection analyses described above indicate that Voyager is approximately 20–30 R_N and 5 R_N from the tangent point during the first and second wave periods, respectively. Parker curvature then leads to negligible errors ($<0.1\ R_N$) in locating the tangent point and determining the shock parameters. Curvature due to magnetic turbulence could produce randomly occurring errors in the tangent point's X position of at most $\pm 3\ R_N$ and $\pm 0.5\ R_N$ for the two wave periods, respectively, assuming in-phase turbulence and using Figures 3 and/or 4. Similar estimates follow for the effects of interference signals in the magnetic field data. The corresponding errors in the a_s and b_s parameters depend sensitively on the particular pair of events considered. However, it is reasonable to equate the random error in a_s with the above errors in the tangent point's location. Comparison with Figure 7 then indicates that curvature effects and interference signals can account for some of the scatter in Figures 7 and 8.

Before proceeding we confirm that independent connection analyses using standard foreshock theory [*Cairns*, 1987*a*; *Fitzenreiter et al.*, 1990] show that the remote-sensing analysis does produce shock parameters consistent with the spacecraft being magnetically connected to the bow shock when the wave events occur. Moreover, the connection analyses demonstrate that even small changes in the shock position and magnetic field direction are sufficient to connect and/or disconnect the spacecraft from the bow shock, consistent with the great time variability in the observed wave data and the generally small variations in the observed magnetic field direction.

6. SHOCK SHAPES AND SPACECRAFT TRAJECTORY

The shape and location of Neptune's bow shock vary significantly with the varying shock parameters shown in Figures 7 and 8. The solid lines in Figure 9 show representative shock shapes inferred from the remote-sensing analysis near times 1100 and 1300 SCET: characteristics $(a_s, b_s) = (42.3, 0.014)$ and $(38.2, 0.008)$, respectively. Voyager 2's trajectory is shown with circles spaced by 30-min time intervals. The two dashed lines show the locations of the MAG and PLS shocks. The remotely sensed shock near 1430 SCET ($a_s \sim 34.3 \pm 0.3\ R_N$ and $b_s \sim 0.008\ R_N^{-1}$) is approximately coincident with the MAG and PLS shocks and is not shown. During the first wave period, 1040–1115 SCET, the shock is inferred to have a relatively elongated shape. After 1255 SCET the shock has an average shape

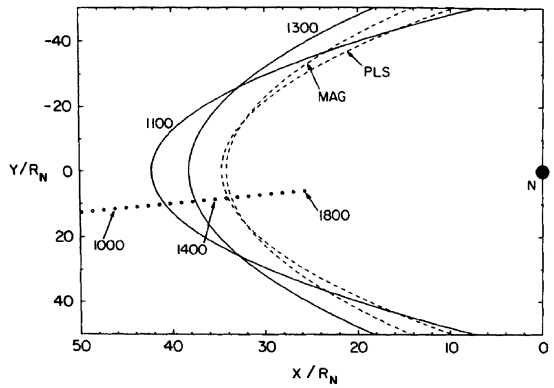

Fig. 9. Comparison of shock shapes inferred from the remote-sensing analysis and the MAG and PLS models. The 1100 SCET shock shape is significantly elongated and narrow compared with the 1300 SCET, MAG and PLS shock shapes. The remotely sensed shock near 1430 SCET lies essentially on the MAG shape and is not shown. As described in the text, the variations in shock shape inferred in the remote-sensing analysis can potentially explain the existence and location of the multiple shock crossings observed outbound from Neptune.

approximately equivalent to the MAG model but a nose position that moves continuously planetward.

Comparison of the shock shapes determined in this paper with the MAG and PLS shock shapes leads to several points. First, Figure 9 indicates that the remotely sensed shock near 1430 SCET and the MAG and PLS models all accurately represent the location of the inbound shock crossing. Second, the variations in remotely sensed shock shape and position shown in Figure 9 imply that Neptune's bow shock moves through huge spatial volumes downstream from the planet. This implies the possibility of multiple shock crossings downstream from the planet along the outbound trajectory, as is indeed observed [*Belcher et al.*, 1989; *Ness et al.*, 1989]. The outbound bow shock crossings are observed in the ranges $-126\ R_N < X < -110\ R_N$ and $115\ R_N < \rho = (Y^2 + Z^2)^{1/2} < 135\ R_N$; for this range of X, shocks with $0.008 < b_s < 0.01\ R_N^{-1}$ have $120\ R_N < \rho < 145\ R_N$, while the relatively elongated shock near 1100 SCET has $100 < \rho < 110\ R_N$. Detailed comparison of the outbound shock crossings with the remote-sensing results requires use of a hyperboloidal shock shape. Nevertheless, the remote-sensing analyses give ranges for the shock parameters that are qualitatively consistent with the existence and locations of the multiple shock crossings observed outbound from Neptune. Flapping motions of the bow shock are, however, the most likely cause for the large number of outbound crossings.

The position of the tangent point on the shock for each connection event, and the distance between the spacecraft and the tangent point, can be estimated using the remotely sensed shock characteristics and a standard connection analysis [*Cairns*, 1987*a*; *Fitzenreiter et al.*, 1990]. During the periods 1040–1115 SCET and 1255–1430 SCET, Voyager was approximately 10 R_N and 5 R_N, respectively, from the tangent point. The continual magnetic connection of the spacecraft to the quasi-perpendicular region of the shock (Figure 5), together with the small distance between the spacecraft and the tangent point, provides a qualitative explanation for the absence of significant energetic foreshock ions [*Krimigis et al.*, 1989] and associated plasma waves upstream from Neptune. At Earth these ions are observed to be associated primarily with magnetic connection to the quasi-parallel regions of the shock [e.g., *Thomsen*, 1985]. Qualitatively, therefore, Voyager's inbound trajectory is not suited for observing such foreshock ions and associated plasma waves.

7. Ram Pressure Effects Versus Dipole Orientation Effects

It is well known that variations in the Mach number and the ram pressure of the solar wind may compress a planet's magnetosphere and cause large-scale variations in the location and shape of planetary bow shocks [e.g., *Spreiter et al.*, 1966; *Binsack and Vasyliunas*, 1968; *Formisiano*, 1979]. When we balance the solar wind ram pressure with the planet's magnetostatic pressure and take into account Mach number effects, the standoff distance a_s of a bow shock is expected to vary according to [*Spreiter et al.*, 1966]

$$a_s \propto \frac{M^2 + 3}{4M^2} (n_{sw} v_{sw}^2)^{-1/6} \tag{5}$$

Here n_{sw} and v_{sw} are the solar wind number density and speed, respectively, and the ratio of specific heats γ is taken to be 5/3. The Mach number M can be identified with the free-stream Mach number v_{sw}/C_S, where C_S is the fluid sound speed, when the Alfvén Mach number is significantly greater than unity [e.g., *Spreiter et al.*, 1966]. Thus the bow shock is moved planetward by higher Mach number and/or higher ram pressure solar wind flows. Equation (5) must be modified when the planet's magnetic dipole is oriented approximately pole-on to the solar wind flow [e.g., *Biernat et al.*, 1981; *Ip and Voigt*, 1985]. However, during the period 1000–1430 SCET of interest here, Neptune's dipole had an approximately Earthlike interaction with the solar wind [*Ness et al.*, 1989, Figure 5].

Solar wind density, velocity, and ram pressure data are available from the Voyager 2 plasma instrument, the PLS instrument [*Bridge et al.*, 1977], courtesy of M. Zhang and J. W. Belcher. Figure 10 compares the time variations in the solar wind ram pressure given by the PLS instrument (in massless units, $n_{sw} v_{sw}^2$) for the period 1000–1500 SCET with the variations in nose position a_s given by the remote-sensing analysis. Since the convection time from Voyager to the shock is only of the order of 5 min and 1 min for the periods 1040–1115 SCET and 1255–1430 SCET, respectively, no time lagging of the ram pressure data is performed in Figure 10. Ram pressure data are shown at two time resolutions; the open circles show L mode ion data with a 48-s time resolution, while the solid triangles show M mode ion data with a 12-min time resolution. During this time period the solar wind speed remained constant to within less than 5%; the variations in ram pressure correspond almost entirely to variations in the number density of the solar wind. The PLS data shown here and by *Belcher et al.* [1989] imply free-stream Mach numbers of the order of 30 and Alfvén Mach numbers increasing from 3.5 ± 0.5 near 1000 SCET to an approximately constant value of 4.3 ± 0.7 between about 1200 SCET and the shock crossing. These Mach numbers are sufficiently large for Mach number effects to be quanti-

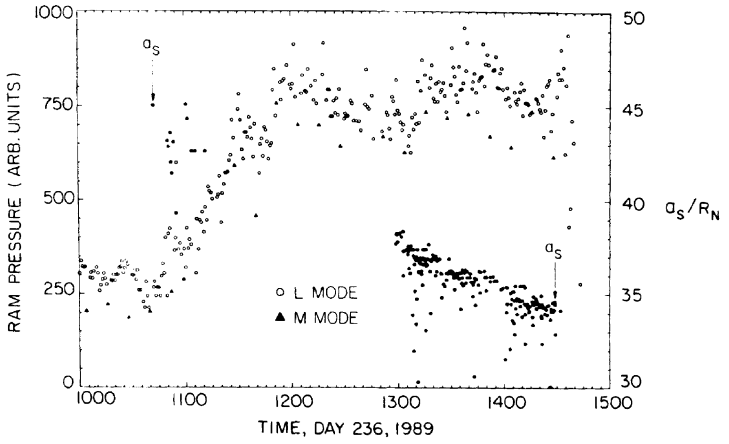

Fig. 10. Comparison of the time histories of the L and M mode ram pressure data from the PLS instrument (open circles and solid triangles, respectively) and the remotely sensed time variations in a_s (solid circles). The solar wind ram pressure increased by a factor of 3.2 from an unusually low level prior to about 1045 SCET to a constant (and typical) level after about 1200 SCET. Location of the shock's nose near 38–43 R_N during the first wave period is consistent with the unusually low observed ram pressure. However, the large-scale planetward motion of the shock during the second wave period is not a response to the constant ram pressure observed (within 15%). Instead, these shock motions are interpreted as evidence for Neptune's rotational phase controlling the location of the bow shock.

tatively unimportant in equation (5) and the remainder of this paper.

The solar wind ram pressure increases by a factor of approximately 3 from 1040 to 1200 SCET and remains approximately constant (within about 15%) from 1200 to 1500. According to equation (5) the bow shock should move closer to the planet as the solar wind ram pressure (and Mach number) increases and should remain stationary when the ram pressure is constant. The remote-sensing analysis infers large-scale, monotonic, planetward motions of the bow shock during the second period of Langmuir wave activity, 1255–1430 SCET. However, this motion occurs while the ram pressure and Mach number are effectively constant. Thus Figure 10 provides a first demonstration that the inferred shock motions from 1255 to 1430 SCET cannot be due to variations in the solar wind ram pressure or Mach number. Instead, an explanation in terms of rotation of Neptune's offset, tilted magnetic dipole is pursued in section 8. Variations in the solar wind ram pressure can, however, explain several aspects of the results from the first wave period, 1040–1115 SCET. First, the low ram pressure in this period implies that the shock should be located unusually far from the planet. Second, the increased ram pressure after 1115 SCET, in conjunction with the magnetic field rotation shown in Figures 3 and 5, naturally explains Voyager's magnetic disconnection from the shock after 1115 SCET.

Quantitative comparisons between the remotely sensed standoff distances of the bow shock and the predictions of equation (5) with the observed ram pressure and Mach number variations are given in Figure 11. The dots and triangles in the figure show the theoretical ratio $a_{th}(t)/a_0$ predicted by (5) using the L and M mode PLS data, respectively. Here the normalization constant a_0 is the average nose position corresponding to the period 1200–1440 SCET of approximately constant ram pressure and Mach number. The remotely sensed nose position a_s, normalized by 38.2 R_N, is shown by the solid circles; this normalization corresponds to the remotely sensed value of a_s near 1300 SCET when the ram pressure first reaches the steady level corresponding to the a_0 parameter and Langmuir waves are observed. Figure 11 shows three important quantitative results. First, equation (5) and the observed variations in ram pressure and Mach number are quantitatively consistent with the bow shock having $a_s \sim 43\ R_N$ for much of the period 1040–1115 SCET, as found using the remote-sensing analysis. For instance, a shock with $a_s = 42.5\ R_N$ near 1040 SCET would have $a_s = 35.0\ R_N$ during the period 1300–1430 SCET of nominal solar wind conditions (the factor of 3.2 increase in ram pressure corresponds to a factor of 1.2 decrease in a_s). Second, the quantitative agreement between these two independent analyses in locating the shock's nose near 43 R_N for the period 1040–1115 SCET argues that the remote-sensing analysis is working correctly. Third, Figure 11 explicitly shows that the monotonic decrease in the remotely sensed a_s parameter after 1255 SCET cannot be understood in terms of variations in the solar wind ram pressure or Mach number. Before proceeding we note that there is one potential difficulty for the 1040–1115 SCET data being interpreted solely in terms of ram pressure variations: the apparent absence of a decrease in the remotely sensed a_s values. Section 8 contains a discussion of this apparent difficulty in terms of sunward expansion of the "base" bow shock.

8. Discussion

We have shown that variations in the solar wind ram pressure and Alfvén Mach number cannot explain the monotonic, 4-R_N decrease in the inferred standoff distance of Neptune's bow shock from 1255 to 1430 SCET, day 236, 1989. Similarly, surface waves on and flapping of the bow shock cannot explain the monotonic nature and long time duration of the inferred planetward motion. *Belcher et al.* [1989], *Ness et al.* [1989], and *Voigt and Ness* [1990] have

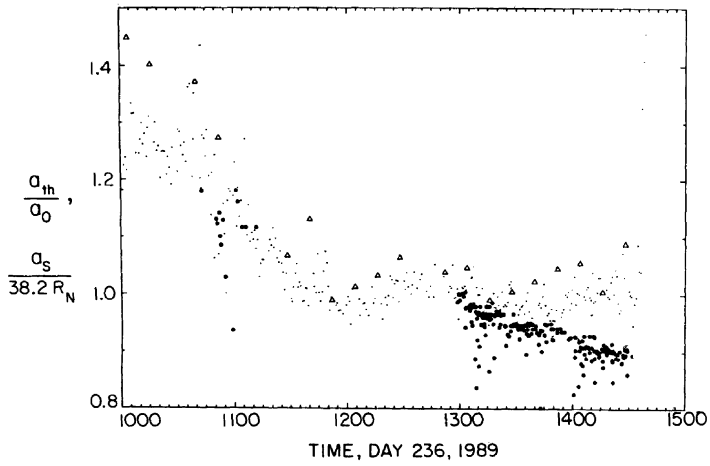

Fig. 11. Comparison of the remotely sensed a_s parameter (solid circles) and the theoretical ratio a_{th}/a_0 based on equation (5) and the L and M mode ram pressure data (dots and triangles, respectively). The normalization constant a_0 corresponds to the almost constant ram pressure after 1300 SCET, while the a_s parameters are normalized by the value 38.2 R_N appropriate to 1300 SCET. The solar wind data are consistent with the shock being located unusually far from the planet during the first wave period, evident for the period 1040–1115 SCET. The different time variations in a_{th} and a_s in this period are evidence for sunward motion of the "base" shock (see text) during this period. The solar wind data are qualitatively and quantitatively unable to account for the monotonic decrease in a_s for the period 1240–1430 SCET. These variations are interpreted instead in terms of Neptune's rotation phase controlling the location of the bow shock.

shown that Neptune's magnetosphere changes from a "pole-on" to an "Earthlike" configuration with Neptune's rotation phase. It is therefore natural to investigate the possibility that the inferred variations in a_s are due to Neptune's rotation phase controlling the location and/or shape of the bow shock.

It is possible, in general, for the remote-sensing analysis to be unable to distinguish between purely planetward motion of the shock and changes in the shock's shape and orientation that mimic planetward shock motions. However, section 5 shows that both the spacecraft positions and magnetic field orientations while wave events are observed, and the long duration of the 1255–1430 SCET wave period, necessitate large-scale variations in the shock's a_s parameter, assuming that the shock is symmetric about the X axis. Even assuming that the shock's axis is inclined relative to the X axis, strong arguments exist that large-scale variations in a_s occur during the period 1040–1430 SCET (see below). In addition, irrespective of the shock's orientation, the observed ram pressure implies that the shock's nose should be unusually far from the planet during the first wave period, consistent with the remote-sensing analyses. We therefore first adopt the simplest interpretation, that the remotely sensed variations in a_s correspond entirely to planetward motion of the shock. Possible changes in the shock's orientation are discussed below.

Shock motions due to ram pressure or Mach number variations can be removed from the remotely sensed a_s parameters using the quantity a_{th}/a_0 calculated in Figure 11 using equation (5) and the PLS data. The term "base" shock refers below to the shock position and shape normalized to the period 1200–1430 SCET in which the ram pressure and Mach number are effectively constant. The bottom panel in Figure 12 displays the calculated variations in the "base" nose location $a_c = 38.2 a_s/a_{th} R_N$ for both wave periods. Only 10 points are plotted because of time averaging of the remotely sensed a_s parameter: three points result from the wave events from 1040 to 1115 SCET, while the remaining seven points are spaced at 15-min intervals in the period 1300–1430 SCET. The arrows are error bars taking into account the scatter in the measured a_s parameters and the ratio a_{th}/a_0 based on the PLS data. Figure 12 shows that the

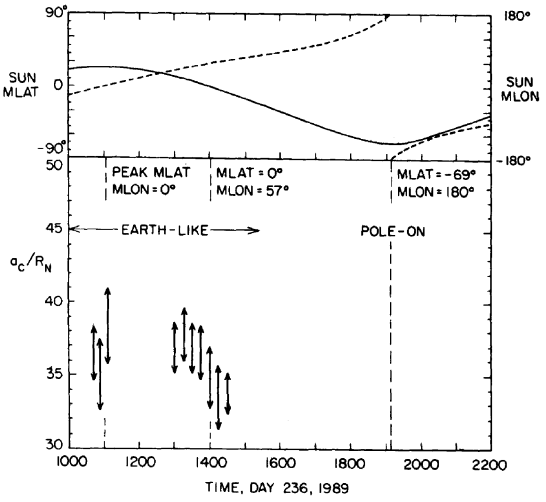

Fig. 12. The bottom panel shows the time history of the nose location a_c of the shock normalized for the observed variations in ram pressure and Mach number using equation (6) and the PLS data. The "base" shock moves sunward from 1040 to 1115 SCET and planetward from 1300 to 1430 SCET, with a maximum standoff distance in the period 1100–1300 SCET. The top panel shows the (Neptunian) magnetic latitude and longitude of the Sun with solid and dashed lines, respectively. The peak in a_c occurs while Neptune's magnetic dipole is nearly perpendicular to the solar wind flow and the Sun's magnetic longitude is in the range 0°–57°.

base shock moves sunward during the first wave period and planetward for almost all the second wave period, with a peak value of a_c inferred during the period 1100–1230 SCET. The base shock moves at least 4 R_N planetward from its peak during the observation period. Since the inferred sunward shock motion during the first wave period depends on averages of Figure 7's widely scattered remote-sensing results, confirmation of the result is desirable. This is obtained by combining Figure 11's ram pressure predictions with the results of Figure 6's conservative remote-sensing analysis in which b_s is required to lie in the range 0.008–0.01 R_N^{-1} (given by the MAG and PLS models and the best remote-sensing estimates). These calculations confirm the results in Figure 12. In particular, the shock moves continuously sunward during the first wave period: from standoff distances in the range 29.7–33.8 R_N at 1040 SCET to 34.1–38.9 R_N at 1112 SCET. Comparisons between the variations in a_c and the rotation phase of Neptune's dipole are also possible using Figure 12. The figure's top panel gives the (Neptunian) magnetic latitude and longitude of the Sun as a function of time. The dipole is exactly perpendicular to the solar wind direction when the Sun's magnetic latitude is zero (near 1402 SCET) and is most "pole-on" to the solar wind when the Sun's magnetic latitude is −69.9° near 1907 SCET [see also *Ness et al.*, 1989]. If the solar wind–dipole interaction is defined to be Earthlike when the dipole is within 20° of being perpendicular to the solar wind direction, the peak in a_c occurs in the Earthlike period. In more detail, the peak in a_c occurs between the times of the Sun having its peak positive magnetic latitude with zero magnetic longitude (1105 SCET) and the time of zero magnetic latitude (perpendicular dipole) with a magnetic longitude of 57° (1402 SCET).

While Figure 12 shows a maximum in the shock's standoff distance near when the dipole is oriented perpendicular to the solar wind flow, there are insufficient upstream data to determine the variation in the standoff distance during an entire Neptunian day. However, the simplest speculative model for the data in Figure 12 involves the shock's standoff distance varying periodially from a single minimum when the dipole is pole-on to a single maximum when the dipole is Earthlike. Future theoretical modeling is necessary for progress on this matter. However, even a theoretical understanding of the data in Figure 12 is not currently available in terms of published theoretical models [e.g., *Olsen*, 1969; *Ip and Voigt*, 1985; *Voigt and Ness*, 1990, and references therein]. For instance, while Voigt's recent calculations (personal communications, 1990, 1991) show that Neptune's subsolar magnetopause distance should vary by a factor of 2 with rotational phase, with a minimum when the dipole is most nearly pole-on, these changes correspond primarily to the indentation of the polar cusp while the overall location of the magnetopause remains effectively constant [*Voigt and Ness*, 1990, Figure 1]. Similarly, *Olsen* [1969] finds that changing the dipole tile angle by 30° from the perpendicular solar wind–dipole case, corresponding to the period 1040–1430 SCET considered here, leads to changes in magnetopause position of only a few percent. Further research is necessary to resolve these questions. It is worthwhile pointing out several potentially important limitations of the available theoretical models for bow shock/magnetopause location and shape. The first limitation is that most theoretical models explicitly address only the structure and location of the magnetopause; little theoretical effort has been devoted to the bow shock itself. Second, the magnetopause size and shape are determined using non-self-consistent analyses that usually neglect the magnetospheric plasma, magnetic flux entry into the magnetosphere (i.e., magnetic reconnection), the plasma flow and magnetic field in the magnetosheath, and the solar wind magnetic field. Third, the effects of time variations in the dipole's orientation, rotationally induced magnetic field components, and time-varying Alfvén wave stresses are neglected in discussing both the magnetopause and the bow shock. There is therefore considerable scope for theoretical efforts intended to explain the results in Figure 12 and the remainder of this paper.

We now consider changes in the orientation of the shock and the corresponding implications for the remotely sensed shock parameters in Figure 7. Both Jupiter [*Engle and Beard*, 1980; *Lepping et al.*, 1981; *Smith and Lee*, 1986] and Venus [*Russell et al.*, 1988; *Zhang et al.*, 1990] are believed to have bow shocks whose shapes and orientation relative to the Sun-planet line vary with time. Changes in the orientation of the dipole, magnetospheric current systems, or the compressibility of the subsolar magnetosphere with Neptune's rotation phase might lead to an asymmetric shock shape aligned on average only with the Sun-Neptune line (ignoring aberration). We therefore considered generalized versions of Figure 5 with the shock's symmetry axis inclined relative to the X direction. For a shock with the MAG/PLS shape inclined at an angle of the order of 10° from the X axis in the $-Y$ direction and a standoff distance of the order of 38.5 R_N the spacecraft trajectory would lie continuously inside the foreshock from approximately 1300 SCET to 1415 SCET. (The observed field orientation requires this standoff distance near 1300 SCET.) Such a model could therefore potentially account for the relatively continuous wave events from 1255 to 1430 SCET without the shock necessarily moving continuously planetward. However, the unaveraged PWS data shown in Figure 2*b* are not consistent with expectations based on Earth data [e.g., *Filbert and Kellogg*, 1979; *Etcheto and Faucheux*, 1984; *Gurnett*, 1985, Figure 11] for a smooth traversal of this static foreshock. In particular, both the presence of multiple stable maxima, deep nulls, and periods of background levels in the data, the correlation of wave maxima and nulls with magnetic field variations, are indicative of excursions into the solar wind and crossings of the upstream foreshock boundary (as considered in the majority of this paper) and not a phenomena in a static, time-invariant foreshock. Thus explanations of these observations in terms of foreshock time variability (not related to shock motions) are required before this static foreshock model can be considered viable. There are three additional reasons why large-scale variations in the shock's a_s parameter are required, even in this model, to explain the wave observations. (1) Increased standoff distances of the order of 42 R_N are required to account for the waves observed from 1040 to 1115 SCET if the above shock orientation and shape are retained. (2) Increasing the shock's inclination angle in the above and the opposite ($+Y$ direction) sense increases and decreases, respectively, the standoff distance required for connection in the first wave period. However, the shock is unlikely to be inclined in the $+Y$ direction during the first wave period (decreased standoff distance) since the shock's orientation angle then varies in the opposite sense to Neptune's rotation. (3) The observed ram pressure variations require significant differences in the base shock's standoff

distance during the two wave periods, except in the unlikely event that the shock has a standoff distance of the order of 46 R_N during the first wave period ($38.5 \times 3.2^{1/6}$). In particular, for the nominal model detailed above, a_c increases from near 34 R_N toward 38 R_N from 1040 to 1115 SCET. In summary, therefore, the Voyager data require large-scale variations in the standoff distance of Neptune's bow shock irrespective of possible changes in the orientation (and shape) of the shock.

Determining the asymmetric characteristics of Neptune's bow shock via the remote-sensing technique requires magnetic connection of the spacecraft to many widely separated parts of the shock. Figure 5 suggests that the Voyager data are unlikely to be well suited to such an analysis. Nevertheless, we generalized the constraint (3) so as to permit the symmetry axis of the shock, as well as the a_s and b_s parameters, to be determined using a least squares technique. The analyses performed to date indicate that the preferred shock solutions have their symmetry axes aligned with the X axis, thereby supporting the analyses performed in sections 5 and 6. Nevertheless, it should be a simple matter to adapt the remote-sensing technique used here to test shock orientations and shapes predicted by future theoretical work.

Voyager's speed is commensurate with the planetward speed of the shock. Thus, presuming that the shock continued to move planetward after the inbound bow shock crossing, consistent with the discussion above, it is likely that the actual thickness of the shock layer, the magnetosheath, and the magnetopause are substantially smaller than those inferred directly from timing measurements. Similarly, given the rotational control of Neptune's magnetosphere argued for above, particular care must be given to properly separating time and spatial variations in the plasma and magnetic field data.

9. CONCLUSIONS

In this paper we have performed a remote-sensing analysis for the location and shape of Neptune's bow shock prior to the inbound bow shock crossing. The analysis uses the magnetic fields and spacecraft positions at the times of specific wave events to fit the bow shock shape to a paraboloid oriented along the X axis with standoff distance a_s and flaring parameter b_s. Comparisons of remote-sensing results with the locations of the inbound and outbound shock crossings, solar wind ram pressure data, and independent connection analyses produce consistent results. Our analyses show that static models for Neptune's bow shock based on shock crossing data [e.g., *Belcher et al.*, 1989; *Ness et al.*, 1989] are not viable. The long time duration, range of spacecraft positions, and number of foreshock encounters during which the Voyager spacecraft observed Langmuir waves along its inbound trajectory require that large-scale motions of Neptune's bow shock occur. Changes in shock orientation can potentially mimic some, but not all, of the inferred shock motions.

The results of this remote-sensing analysis are as follows: (1) Large-scale motions of the bow shock occur while Voyager is upstream from the inbound bow shock. In detail, the nose of the bow shock moves between 43 R_N and 34 R_N during the period 1040–1430 SCET. (2) The nose of the bow shock moves monotonically planetward during the second period of wave activity (1255–1430 SCET). (3) The inferred shock speed is commensurate with (although smaller than) the spacecraft speed. (4) The remotely sensed shock parameters are consistent with the location of the inbound bow shock. (5) The best estimate of the shock's average flaring parameter b_s is $0.008 \pm 0.002\ R_N^{-1}$. This agrees very well with the MAG and PLS models based on the inbound and outbound shock locations. (6) Weak evidence exists for the shock's b_s parameter being of the order of $0.014\ R_N^{-1}$ during the first wave period. This may be a systematic bias due to shock motions. Biases due to shock motion and the magnetic field orientation affect most determinations of b_s during the second wave period. (7) Location of the bow shock near 38–43 R_N during the first period of wave activity is consistent with the low solar wind ram pressure observed. (8) The remotely sensed continual, planetward motion of the shock during the second period of wave activity occurs while the solar wind ram pressure and Mach number are effectively constant. This shock motion is interpreted in terms of the shock location being controlled by the rotation phase of Neptune's oblique, tilted magnetic dipole. (9) Normalizing by the solar wind ram pressure and Mach number according to the conventional *Spreiter et al.* [1966] formula, the nose of the "base" shock is found to move sunward from 1040 to 1115 SCET and planetward from 1240 to 1430 SCET, with a maximum being inferred in the period 1100–1330 SCET.

The maximum standoff distance of the base shock occurs while Neptune's magnetic dipole is close to being perpendicular to the solar wind flow. No theoretical explanation for the corresponding motions of the base shock is currently available. Similarly, the dipole orientation for the shock's minimum standoff distance is not known; however, the simplest model involves the dipole being "pole-on" at this time. We suggest that our analyses are consistent with rotational control of the location and perhaps the shape of Neptune's bow shock. Changes in the orientation of the shock may exist but have not been addressed in detail here. If correct, rotational control of the bow shock's location, together with the inferred planetward shock motion after the inbound shock crossing, implies that investigations of Neptune's magnetosheath and magnetopause must take great care to resolve time and spatial variations in the plasma and field data. The above results, as well as possible future remote-sensing analyses investigating changes in the shock's orientation, will provide suitable tests for detailed theoretical models of Neptune's bow shock/magnetosphere system.

The foregoing results have illustrated the usefulness of remote-sensing techniques using Langmuir waves for detailed investigations of the location and motions of planetary bow shocks. Methods of adapting these techniques for situations with interference-contaminated data have been developed and used successfully here. As should be expected, however, suitable plasma wave, magnetic field, and spacecraft location data must be available for a successful and complete analysis to be possible. In the future we hope to use these remote-sensing techniques to investigate other planetary bow shocks, as well as interplanetary shocks.

APPENDIX: THEORETICAL STRUCTURE OF THE ELECTRON FORESHOCK

This appendix describes the theoretical structure of the foreshock with a view to explaining the expected finite width of the region containing high levels of Langmuir waves. As discussed by *Filbert and Kellogg* [1979] and *Cairns* [1987*a*,

b], the beam speed of the streaming electrons is a function of position in the foreshock. The electrons move under the influence of the solar wind magnetic field and the solar wind convection electric field **E**. These fields result in a gyrocenter velocity composed of the electron velocity parallel to the magnetic field and an **E** × **B** drift velocity perpendicular to the magnetic field. This drift velocity always has a component directed in the antisunward, or shockward, direction. Electrons leaving each point on the shock must then have a minimum parallel velocity, the so-called cutoff velocity v_c (which varies with position), to escape upstream from the local shock surface. These cutoff speeds map into the foreshock along the particle characteristics and lead to the foreshock distribution functions having an abrupt cutoff at the local v_c: shock-accelerated electrons at the observation position must have $v_\parallel > v_c$. Growth of Langmuir waves tends to smooth out the cutoff distribution, leading to a more conventional beam feature with $v_b \sim v_c$. Defining an angle θ between the tangent magnetic field line and the line joining the observation position to the tangent point, the beam speed is approximately

$$v_b = \frac{v_{sw} \sin \theta_{vB}}{\tan \theta} \tag{6}$$

Here θ_{vB} is the angle between the magnetic field and the solar wind velocity v_{sw} defined by $\mathbf{v}_{sw} \cdot \mathbf{B} = v_{sw} B \cos \theta_{vB}$. The beam instability is expected to produce strong levels of waves only when the beam speed exceeds about, say, five electron thermal speeds V_e: $v_b > 5V_e$. During Voyager 2's passages through Neptune's foreshock the PLS data give $v_{sw} \sim 400$ km s^{-1} and $V_e \sim 420$ km s^{-1} assuming $T_e = 2T_i \sim 1$ eV. The maximum expected width of Neptune's electron foreshock, measured from the tangent field line, is then less than 10°.

Acknowledgments. The magnetic field data and PLS data used in this paper were provided by Norman Ness and Ron Lepping, and John Belcher and Ming Zhang, respectively. I.H.C. and C.W.S. gratefully acknowledge receipt of unpublished material from and conversations with Hannes Voigt. I.H.C. thanks Larry Granroth and Scott Allendorf for their frequent help on computer matters. Unusually insightful comments from a referee were of particular help in revising and strengthening the paper. The authors acknowledge financial support from NASA contract 957723 with JPL and NASA grant NAGW-2040 with NASA Headquarters at the University of Iowa, NASA contract 957921 with JPL at the Bartol Research Institute, and NASA contract 957805 at TRW.

The Editor thanks M. F. Thomsen and two other referees for their assistance in evaluating this paper.

REFERENCES

Anderson, R. R., G. K. Parks, T. E. Eastman, D. A. Gurnett, and L. A. Frank, Plasma waves associated with energetic particles streaming into the solar wind from the Earth's bow shock, *J. Geophys. Res.*, *86*, 4493, 1981.

Behannon, K. W., M. H. Acuna, L. F. Burlaga, R. P. Lepping, N. F. Ness, and F. M. Neubauer, Magnetic field experiment for Voyagers 1 and 2, *Space Sci. Rev.*, *21*, 235, 1977.

Belcher, J. W., et al., Plasma observations near Neptune: Initial results from Voyager 2, *Science*, *246*, 1478, 1989.

Biernat, H., N. Kömle, and H. Rucker, Analytical two-dimensional model for a pole-on magnetosphere, *Planet. Space Sci.*, *29*, 1101, 1981.

Binsack, J. H., and Y. M. Vasyliunas, Simultaneous IMP 2 and OGO 1 observations of bow shock compressions, *J. Geophys. Res.*, *73*, 429, 1968.

Bridge, H. S., J. W. Belcher, R. J. Butler, A. J. Lazarus, A. M. Mauretic, J. D. Sullivan, G. L. Siscoe, and V. M. Vasyliunas, The plasma experiment on the 1977 Voyager mission, *Space Sci. Rev.*, *21*, 259, 1977.

Cairns, I. H., The electron distribution function upstream from the Earth's bow shock, *J. Geophys. Res.*, *92*, 2315, 1987*a*.

Cairns, I. H., A theory for the Langmuir waves observed upstream from the Earth's bow shock, *J. Geophys. Res.*, *92*, 2329, 1987*b*.

Engle, I. M., and D. B. Beard, Idealized Jovian magnetosphere and field, *J. Geophys. Res.*, *85*, 579, 1980.

Etcheto, J., and M. Faucheux, Detailed study of electron plasma waves upstream of the Earth's bow shock. *J. Geophys. Res.*, *89*, 6631, 1984.

Filbert, P. C., and P. J. Kellogg, Electrostatic noise at the plasma frequency beyond the Earth's bow shock, *J. Geophys. Res.*, *84*, 1369, 1979.

Fitzenreiter, R. J., J. D. Scudder, and A. J. Klimas, Three-dimensional analytical model for the spatial variation of the foreshock electron distribution function: Systematics and comparisons with ISEE observations, *J. Geophys. Res.*, *95*, 4155, 1990.

Formisiano, V., Orientation and shape of the Earth's bow shock in three dimensions, *Planet. Space Sci.*, *27*, 1151, 1979.

Fuselier, S. A., D. A. Gurnett, and R. J. Fitzenreiter, The downshift of electron plasma oscillations in the electron foreshock region, *J. Geophys. Res.*, *90*, 3935, 1985.

Fuselier, S. A., W. C. Feldman, S. J. Bame, E. J. Smith, and F. L. Scarf, Heat flux observations and the location of the transition region boundary of Giacobini-Zinner, *Geophys. Res. Lett.*, *13*, 247, 1986.

Gurnett, D. A., Plasma waves and instabilities, in *Collisionless Shocks in the Heliosphere: Reviews of Current Research, Geophys. Monogr. Ser.*, vol. 35, edited by B. T. Tsurutani and R. G. Stone, p. 207, AGU, Washington, D. C., 1985.

Gurnett, D. A., W. S. Kurth, and F. L. Scarf, Plasma waves near Saturn: Initial results from Voyager 1, *Science*, *212*, 235, 1981*a*.

Gurnett, D. A., J. E. Maggs, D. L. Gallagher, W. S. Kurth, and F. L. Scarf, Parametric interaction and spatial collapse of beam-driven Langmuir waves in the solar wind, *J. Geophys. Res.*, *86*, 8833, 1981*b*.

Gurnett, D. A., W. S. Kurth, F. L. Scarf, and R. L. Poynter, First plasma wave observations near Uranus, *Science*, *233*, 106, 1986.

Gurnett, D. A., et al., First plasma wave observations at Neptune, *Science*, *246*, 1494, 1989.

Ip, A. K., and G.-H. Voigt, Plasma-dominated magnetic field configurations for the magnetosphere of Uranus, *J. Geophys. Res.*, *90*, 6287, 1985.

Klimas, A. J., The electron foreshock, in *Collisionless Shocks in the Heliosphere: Reviews of Current Research, Geophys. Monogr. Ser.*, vol. 35, edited by B. T. Tsurutani and R. G. Stone, p. 237, AGU, Washington, D. C., 1985.

Krimigis, S. M., et al., Hot plasma and energetic particles in Neptune's magnetosphere, *Science*, *246*, 1483, 1989.

Lacombe, C., A. Mangeney, C. C. Harvey, and J. D. Scudder, Electron plasma waves upstream of the Earth's bow shock, *J. Geophys. Res.*, *90*, 73, 1985.

Lepping, R. P., L. F. Burlaga, L. W. Klein, J. M. Jessen, and C. C. Goodrich, Observations of the magnetic field and plasma flow in Jupiter's magnetosheath, *J. Geophys. Res.*, *86*, 8141, 1981.

Moses, S. L., F. V. Coroniti, C. F. Kennel, W. S. Kurth, and D. A. Gurnett, Comparison of plasma wave measurements in the bow shocks at Earth, Jupiter, Saturn, Uranus, and Neptune, *Geophys. Res. Lett.*, *17*, 1653, 1990.

Ness, N. F., M. H. Acuna, L. F. Burlaga, J. E. P. Connerney, R. P. Lepping, and F. N. Neubauer, Magnetic fields at Neptune, *Science*, *246*, 1473, 1989.

Olsen, W. P., The shape of the tilted magnetopause, *J. Geophys. Res.*, *74*, 5642, 1969.

Russell, C. T., E. Chou, J. G. Luhmann, P. Gazis, L. H. Brace, and W. R. Hoegy, Solar and interplanetary control of the location of Venus' bow shock, *J. Geophys. Res.*, *93*, 5461, 1988.

Russell, C. T., R. P. Lepping, and C. W. Smith, Upstream waves at Uranus, *J. Geophys. Res.*, *95*, 2273, 1990.

Scarf, F. L., and D. A. Gurnett, A plasma wave investigation for the Voyager mission, *Space Sci. Rev.*, *21*, 289, 1977.

Scarf, F. L., R. W. Fredericks, L. A. Frank, and M. Neugebauer,

Nonthermal electrons and high-frequency waves in the upstream solar wind, 1, Observations, *J. Geophys. Res., 76*, 5126, 1971.

Scarf, F. L., D. A. Gurnett, and W. S. Kurth, Jupiter plasma wave observations: An initial Voyager 1 overview, *Science, 204*, 991, 1979.

Smith, C. W., and M. A. Lee, Coupled wave excitation and ion acceleration upstream of the Jovian bow shock, *J. Geophys. Res., 91*, 81, 1986.

Spreiter, J. R., A. L. Summers, and A. Y. Alksne, Hydromagnetic flow around the magnetospheres, *Planet. Space Sci., 14*, 233, 1966.

Thomsen, M. F., Upstream suprathermal ions, in *Collisionless Shocks in the Heliosphere: Reviews of Current Research, Geophys. Monogr. Ser.*, vol. 35, edited by B. T. Tsurutani and R. G. Stone, p. 253, AGU, Washington, D. C., 1985.

Voigt, G.-H., and N. F. Ness, The magnetosphere of Neptune: Its response to daily rotation, *Geophys. Res. Lett., 17*, 1705, 1990.

Zhang, T.-L., J. G. Luhmann, and C. T. Russell, The solar cycle dependence of the location and shape of the Venus bow shock, *J. Geophys. Res., 95*, 14,961, 1990.

I. H. Cairns, D. A. Gurnett, and W. S. Kurth, Department of Physics and Astronomy, University of Iowa, Iowa City, IA 52242.

S. Moses, TRW Space and Technology Group, 1 Space Park, Redondo Beach, CA 90278.

C. W. Smith, Bartol Research Institute, University of Delaware, Newark, DE 19716.

(Received January 31, 1991;
revised July 22, 1991;
accepted July 22, 1991.)